2026 IEEE International Conference on Robotics and Automation (ICRA 2026)
June 1-5, 2026. Vienna, Austria

A Magnetic-Wheeled Inspection Robot for Interior Corner Traversal

Paul Nadan[1], Jai Kumar[2], Nate Klein[3], Jesse Wallace[3], Hairong Wang[4], Alexander Hakim[3], Adam Dassey[5], Thomas Hoelen[5], Gregory V. Lowry[4], and Aaron M. Johnson[3]

***Abstract*— Automated inspection of steel structures using magnetic climbing robots can reduce costs and improve safety, but many such structures feature interior corners that are challenging for wheeled or tracked robots to traverse. We present the first magnetic-wheeled robot to use X-ray fluorescence for steel structure inspection, Sally, capable of overcoming all interior corner transition types, traversing small obstacles, and maneuvering in tight spaces. By re-purposing its steering and sensor deployment mechanisms, the robot is able to transition back and forth between a steel wall and an adjacent steel ceiling, steel wall, or any floor. We analyze the feasibility of these interior corner transitions and validate the results through experimental demonstrations with Sally. We also demonstrate line scanning, a continuous surface measurement technique enabled by the wheeled design that estimates the average element concentrations along a line, and show it provides greater accuracy and efficiency in both simulation and robot trials compared to the traditional grid point measurement method. Finally, we discuss lessons learned from a field test of Sally at an industrial site.**

I. Introduction

In recent years, magnetic climbing robots have been developed for inspection and maintenance tasks on a wide variety of steel structures including bridges [1], pipes [2], storage tanks [3], and ship hulls [4]. Robotic inspection can eliminate the need to construct costly scaffolding and send human inspectors into potentially hazardous environments. However, robotic locomotion on these structures can be challenging; for instance, the interior of an oil tanker contains several small obstacles, such as rivets, cables, and pipes, as well as interior corners between the floor, walls, and ceiling of the tank. These corner transitions are especially difficult for wheeled and tracked robots because the robot must overcome the magnetic adhesion with the previous surface. Inspection robots may also need to carry bulky sensor payloads. In particular, portable X-ray fluorescence (pXRF) sensors are often used by human inspectors to determine the elemental composition of a surface. While automated pXRF inspection been explored for soil remediation [5,6], this sensing technology also holds great promise for detecting components of interest such as lead or mercury on steel structures.

Aerial robots are often used for visual inspection and researchers have developed perching solutions to enable close-range measurements [7]. However, aerial robots struggle with large payloads, limited runtimes, and confined environments. Tracked climbers can support larger payloads due to the greater surface area of the treads, as in [8], but typically have difficulty traversing larger obstacles. Legged climbers [9,10] or hybrid solutions [11–13] can potentially traverse the widest range of obstacles using switchable adhesion and dexterous limbs, but at the cost of increased complexity and reduced payload. A legged morphology would also make continuous line scanning, discussed below, more challenging. In contrast, wheeled robots can use passive suspensions [1], active suspensions [14], or swiveling magnets [15] to traverse corners and obstacles while maintaining wheel contact, but have thus far been too small to carry a bulky payload like a pXRF sensor and unable to transition to non-ferrous surfaces. A recent exception is found in [16], but this design requires dedicated mechanisms to break contact during transitions.

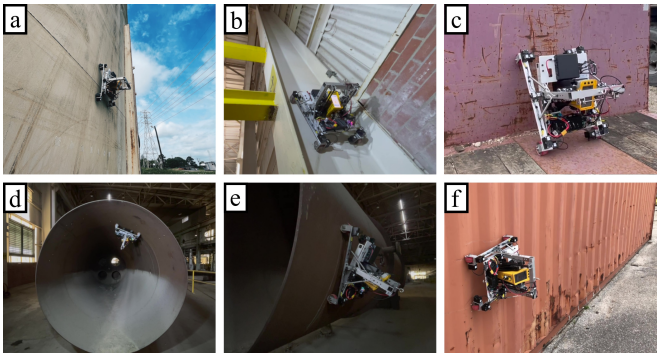

Fig. 1. Images taken of Sally at various locations around an industrial site. a) water storage tank, b) I-beam, c) truck bed, d) 1.8 m metal pipe interior, e) 1.8 m metal pipe exterior, f) shipping container.

Beyond the capabilities of sensor and robotic technology, the sampling method significantly affects the accuracy and efficiency of inspection tasks. Traditionally, this process involves human inspectors physically climbing inside the structure to perform grid point measurements in several locations within a designated area, the mean of these samples representing the average level of a component of interest in that area [17–19]. However, with many sensors, including pXRF, a moving-while-sensing sampling method (line scanning) facilitated by robotic movement presents a more accurate and efficient alternative. This concept has been applied in pipe inspection tasks such as erosion detection and thickness measurement using ultrasonic, PEC, or IR laser probe sensors [20–22]. Line scanning can cover a larger area in the same amount of time, potentially offering a more accurate area mean estimate of the component of interest.

In this work we present Sally (Fig. 1), the first magnetic-wheeled robot to carry a pXRF sensor for steel structure inspection. Sally can overcome all 90° interior corner transi-

[1]Robotics Institute, [2]Electrical and Computer Engineering, [3] Mechanical Engineering, [4] Civil and Environmental Engineering, Carnegie Mellon University, Pittsburgh, PA 15213, USA, [5] Chevron Corporation
pnadan@alumni.cmu.edu, amj1@andrew.cmu.edu

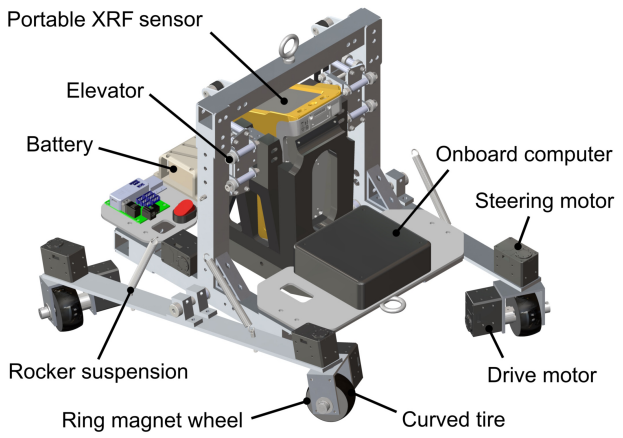

Fig. 2. An annotated visualization of the Sally robot design.

tion types, traverse small obstacles up to 5 cm in height, and maneuver in tight spaces. We analyze the feasibility of various interior corner transitions, determining a set of design constraints that apply to all magnetic-wheeled robots with similar morphology. We find that no single set of parameters can enable a robot to accomplish all transition types unaided, but by re-purposing steering and sensor deployment mechanisms Sally is able to achieve all transition types without adding dedicated mechanisms. We evaluate Sally's capabilities in both a controlled laboratory setting and a realistic field environment. Furthermore, two sampling methods (line scanning and grid point measurement) are compared in simulated, lab, and field trials. We conclude that line scanning offers a more accurate and time-efficient way to estimate element distributions on surfaces like industrial tanks, pipes, or hulls.

II. Robot Design

Sally is an 8.3 kg magnetic-wheeled robot designed to drive on any surface orientation (e.g. floors, walls, and ceilings), maneuver in tight spaces, transition across 90° interior corners, and traverse small obstacles such as pipes and rivets. Sally measures 46 cm long by 35 cm wide, not including the rotating wheel assemblies, and drives on level ground at 0.2 m/s (0.44 body lengths per second). An onboard Intel NUC 11 computer and 3S 5000 mAh LiPo battery enable the robot to operate untethered. Dynamixel XM430-W210T servos are used for all actuators on the robot. Several key features of the design are enumerated below.

1) Magnetic Wheels: Sally's wheels each consist of a single radially polarized ring magnet (manufactured by SDM Magnetics Co.), with a keyed central hole for mounting to an axle. Each magnet is 5 cm in diameter, weighs 350 g, and provides up to 30 kg (294 N) of adhesive force on steel surfaces. In general, wheeled robots can either rely on magnetic wheels or magnets fixed to the base of the robot for adhesion. While fixed magnets offer greater flexibility for the magnet form-factor, magnetic wheels can remain in contact with the surface to provide consistent adhesion as the robot traverses obstacles. Magnetic wheels can be constructed by mounting several magnets around the rim of a wheel, as in [23], but this results in varying magnetic strength as the wheel rotates, especially for low numbers of magnets. Other robots rely on ring magnets which exert a constant force as the wheel rotates, as in [14].

2) Curved Tires: The tires each consist of a curved 3D printed shell that is press-fit around the magnet itself to provide a curved profile, and then wrapped in rubber grip tape to improve traction and dampen impacts. The shell is 2 mm thick at its widest point, and reduces the adhesive force of the wheels on steel to 60 N each. Sally's total mass is 8.3 kg, so this gives an adhesion-to-weight ratio of 2.9. Empirical measurements place the grip tape coefficient of friction at approximately 0.8 on steel and 1.0 on paint, although the friction coefficient gradually decreases over time as the tape experiences wear and accumulates dirt. The curved profile of the tires provides multiple benefits. First, the curvature reduces the size of the contact patch, making it easier to turn the wheel in place when steering. Secondly, the curvature reduces the variation in magnetic force as the wheel is tilted, ensuring consistent adhesion when traversing curved surfaces or obstacles. The adhesive force of a radial ring magnet decreases with distance from the surface and angle relative to the surface [14], so the curved profile reduces the distance at larger angles to partially cancel out these two effects.

3) Rocker Suspension: Attached to each side of the frame is a freely rotating, 46 cm long aluminum rocker plate. A pair of 0.58 N/mm springs connect each rocker plate to the central body to keep the frame roughly aligned with the rockers. The frame has 7.6 cm of ground clearance when the rockers are level, and the length of the rockers ensures that each wheel can be raised above the base of the frame when going over an obstacle. This passive suspension ensures that all four wheels can remain contact with the terrain at all times without any active effort by the robot. While an active suspension could also be used, the extra weight and control complexity make it less desirable than the passive suspension which achieves the goal of enabling obstacle traversal without needing precise sensing and control.

4) Independent Drive and Steering: The four steering motors are mounted at the ends of the two rocker plates, directly connected to the wheel brackets. Each wheel is supported by a U-shaped aluminum bracket with a drive motor mounted on one side. The ability to independently steer all four wheels enables the robot to move with any desired translation and rotation on the surface, including turning in place. This maneuverability helps Sally to navigate tight spaces and closely spaced obstacles; in contrast, a robot with only two independently steered wheels would have a non-zero turning radius and be unable to move laterally. In addition, when the robot is holding position on a vertical surface the wheels can be turned perpendicular to gravity, allowing the robot to hold position indefinitely without exerting torque. This is especially useful because pXRF measurements take 30-90 seconds, so reducing power usage during these measurements greatly extends the robot's battery life. Finally, during interior corner transitions, the rear wheels can be twisted to help break contact with the

previous surface (Section III-B).

5) Portable X-Ray Fluorescence Sensor and Elevator: The robot carries a Vanta pXRF sensor to analyze the surface elemental composition. The pXRF sensor is mounted on a moving carriage, which connects to the robot's frame through a pair of sliders. The sliders are constructed with ball bearings that contact three faces of the rails, constraining the carriage's motion to one axis. A pair of independently driven belts translate the sensor up and down, so that the sensor can be raised clear of any obstacles or lowered to make contact with the surface. The carriage's range of motion goes from 2 cm below the driving surface to 7 cm above it, allowing Sally to scan areas that are not level with the wheels. The ability to extend below the driving surface also allows the carriage to press against the ground, aiding with interior corner transitions (Section III-B). Four omni-wheels are mounted around the base of the sensor to reduce friction during line scanning and overcome small obstacles.

III. Interior Corner Transitions

A. Transition Model

In [24], Fischer et al. present a model for a magnetic-wheeled robot undergoing an interior corner transition and estimate the required wheel friction coefficient. Their analysis focuses on relatively small robots, for which the wheels are large relative to the robot body and the magnet adhesion force is many times greater than the robot weight. A similar model for interior corner transitions is presented in [25], but focuses only on one robot configuration and one surface friction condition. In contrast, here we examine how the required friction coefficient scales with robot weight relative to the magnetic adhesion force, and additionally consider transitions between non-ferrous and ferrous surfaces.

We consider a wheeled robot characterized by the following dimensionless parameters:

$$K = \frac{mg}{2f_m}, \qquad A = \frac{h}{\ell} \tag{1}$$

Where m is the robot mass, g is the gravitational acceleration, f_m is the adhesive force of a single wheel pair (e.g. front or back), ℓ is the distance between the wheel axes, and h is the distance from the center of mass to the bottom of the wheels. We refer to K as the weight ratio and A as the aspect ratio. The following constraints are imposed on the robot parameters:

$$K < 1 \tag{2}$$

$$KA < \frac{1}{2} \tag{3}$$

The constraint in (2) ensures that the magnetic force from the wheels is strong enough to allow the robot to hang inverted from the ceiling, and (3) is the moment balance about the rear wheels which ensures that the robot can drive vertically on a wall without losing adhesion.

In order to simplify the analysis, we assume that the wheel radius is small relative to the size of the robot and that the center of mass is horizontally centered between the two wheels. We further assume that the transition is performed quasi-statically at low speed between perpendicular surfaces.

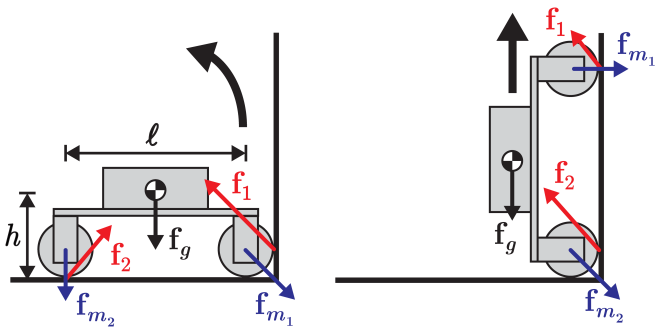

Fig. 3. A free-body diagram of a magnetic-wheeled robot at the moment of front wheel (left) and rear wheel (right) floor-to-wall transition.

To determine the friction conditions necessary to perform an interior corner transition, we examine the transition in two stages: the front wheel transition and the rear wheel transition (Fig. 3). In each case, at the moment of transition the contact force between the specified wheel and the surface it is leaving is zero. We can express the condition of static equilibrium as the vector equations:

$$0 = \mathbf{f}_1 + \mathbf{f}_{m_1} + \mathbf{f}_2 + \mathbf{f}_{m_2} + m\mathbf{g} \tag{4}$$

$$0 = \mathbf{r}_1 \times (\mathbf{f}_1 + \mathbf{f}_{m_1}) + \mathbf{r}_2 \times (\mathbf{f}_2 + \mathbf{f}_{m_2}) \tag{5}$$

Where $\mathbf{f}_1$ and $\mathbf{f}_2$ are the front and rear contact force vectors, $\mathbf{r}_1$ and $\mathbf{r}_2$ are the position vectors of the front and rear wheels relative to the center of mass, $\mathbf{f}_{m_1}$ and $\mathbf{f}_{m_2}$ are the magnetic force vectors acting on the front and rear wheels (combining the magnetic force on each wheel to multiple surfaces as needed), and $\mathbf{g}$ is the gravitational acceleration vector.

We decompose each contact force $\mathbf{f}_i$ into tangential and normal components T_i and N_i and expand (4)–(5) for the front wheel transition,

$$0 = -N_1 + f_m + T_2 + mg_x \tag{6}$$

$$0 = T_1 + N_2 - 2f_m + mg_y \tag{7}$$

$$0 = \frac{\ell}{2}(T_1 - N_2) + h(N_1 + T_2 + f_m) \tag{8}$$

and rear wheel transition,

$$0 = -N_1 - N_2 + 2f_m + mg_x \tag{9}$$

$$0 = T_1 + T_2 - f_m + mg_y \tag{10}$$

$$0 = h(T_1 + T_2 - f_m) + \frac{\ell}{2}(N_1 - N_2) \tag{11}$$

Where all normal forces $N_i \geq 0$.

Our goal is to find the minimum wheel friction coefficient μ for which neither wheel will slip during the transition. We assume that this will occur when both wheels are at the friction limit:

$$\mu = \frac{T_1}{N_1} = \frac{T_2}{N_2} \tag{12}$$

We analytically solve (6)–(8) or (9)–(11) together with (12) for $\mathbf{f}_1$ and $\mathbf{f}_2$ in terms of K for varying values of A and $\mathbf{g}$ using the MATLAB Symbolic Math Toolbox. Equations (2) and (3) are treated as assumptions. Note that (12) is nonlinear

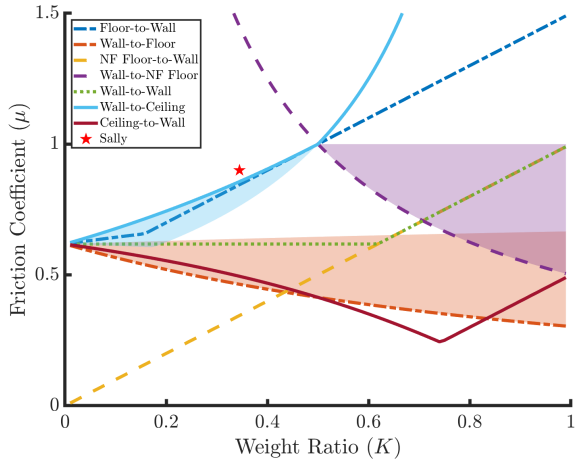

Fig. 4. Minimum required tire friction coefficient as a function of normalized robot weight for each type of 90° interior corner transition. For each transition, the maximum of the front wheel and rear wheel transitions at each weight ratio is taken as the minimum required friction. Transitions are plotted at an aspect ratio of 0, with shaded regions indicating how the friction conditions change up to an aspect ratio of 0.5.

in the force components, preventing the problem from being solved as a linear system of equations.

We also consider two special cases. First, transitions involving a non-ferrous floor are possible since no magnetic force is required to keep the robot on the driving surface. For non-ferrous-floor-to-wall and wall-to-non-ferrous-floor transitions, the appropriate $\mathbf{f}_m$ terms are set to zero.

The other case we consider is a wall-to-wall transition. In a wall-to-wall transition, gravity is parallel to both surfaces, and therefore does not act in the direction of either the normal or the tangential contact forces. Since our model only considers in-plane forces, the wall-to-wall solutions effectively assume no out-of-plane forces or moments, which is equivalent to assuming that the aspect ratio (or height) of the robot is zero.

The results of this analysis are shown in Fig. 4 for all common transitions. We observe that the wall-to-non-ferrous-floor transition is the most difficult transition type at low values of K, while the floor-to-wall and wall-to-ceiling transitions are the most difficult at high K values. At the crossover point $K = \frac{1}{2}$, an infeasibly high friction coefficient of 1.0 is required, revealing that no robot of this morphology can achieve all transition types unaided. We also observe that a friction coefficient of $\frac{1-\sqrt{5}}{2} \approx 0.62$ is the minimum required to complete all transitions between ferrous surfaces as the magnetic adhesion force approaches infinity ($K = 0$).

B. Transition Strategies

Examining the approximate location of Sally on the plot in Fig. 4 ($K = 0.345$, $\mu = 0.9$), we predict that wall-to-non-ferrous-floor transitions will be infeasible, while floor-to-wall and wall-to-ceiling transitions are borderline depending on the freshness of the wheel grip tape. However, the presence of additional actuators on the robot for sensor deployment and steering can enable Sally to circumvent these limits.

During a front wheel transition, Sally can press the pXRF elevator into the surface to produce an additional vertical force near the center of the robot, helping to pry the front wheels free and reducing the required friction coefficient. In this case, Equations (4) and (7) are modified to include the force $\mathbf{f_p}$ from the pXRF elevator.

$$0 = \mathbf{f}_1 + \mathbf{f}_{m_1} + \mathbf{f}_2 + \mathbf{f}_{m_2} + \mathbf{f}_p + m\mathbf{g} \tag{13}$$

$$0 = T_1 + N_2 - 2f_m + f_p + mg_y \tag{14}$$

Similarly, during a rear wheel transition, Sally can use the independent steering motors to twist the rear wheels sideways. This has two effects: first, magnetic adhesion force diminishes at larger angles relative to the surface, making it easier to break free. Second, as the wheel twists, the side of the wheel bracket comes into contact with the surface, so the torque applied by the steering motor generates an additional contact force pushing the robot away from the wall.

For each transition, using the pXRF to push off of the wall reduces the friction coefficient necessary to complete a front wheel transition (Fig. 5). For each starting surface (ferrous and non-ferrous floors, wall, or ceiling), there are different limiting conditions on the maximum force that the pXRF can apply before the robot can no longer stay on that surface. In Fig. 5, the curves for transitions cut off at the point where the pXRF force would cause Sally to fail the transitions. For all front wheel transitions, one failure condition is if the rear wheels lose contact with the initial surface. Solutions are filtered out if the normal force corresponding to the real wheel contact is negative.

The wall-to-wall and wall-to-ceiling transitions can also fail if the robot starts to slide down the wall. The pXRF force decreases the normal force on the wheels, which reduces the frictional force they can apply and potentially causes the robot to slip. For wall-to-wall transitions, the necessary conditions to avoid sliding are

$$N_1 \geq \frac{mg}{2\mu}, \qquad N_2 \geq \frac{mg}{2\mu} \tag{15}$$

For wall-to-ceiling transitions, the limiting condition to avoid sliding is best expressed in terms of the weight ratio and the normalized pXRF force $P = \frac{f_p}{2f_m}$.

$$P \leq 1 - \frac{1}{\mu}(K - \frac{1}{2}) \tag{16}$$

In cases where $K < \frac{1}{2}$ (such as Sally), the robot is light enough that the magnetic force between the front wheels and the ceiling is sufficient to hold the robot up, so the sliding failure mode can be safely ignored.

C. Transition Control

An additional challenge arises during certain transitions that is not captured by the above static analysis. As the robot moves across a transition, the relative speeds of the wheels relative to the surfaces change due to the corner geometry, with the rear wheels stationary at the start of the transition, the front wheels stationary at the end, and the wheel speeds equal at the halfway point. This presents a problem if the wheels are velocity controlled, because the front wheels will tend to pull the rear wheels free from the

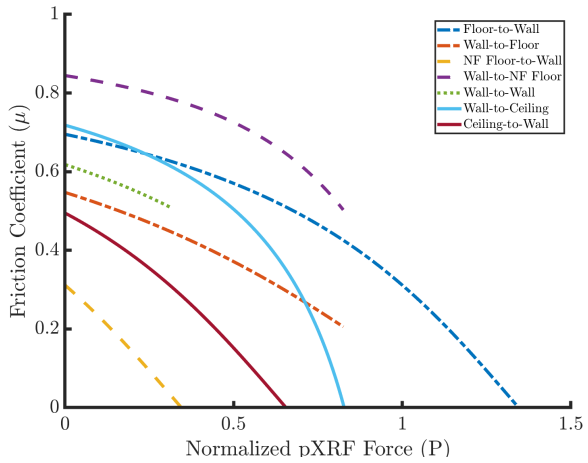

Fig. 5. The required friction coefficient for each front-wheel transition as force is applied with the pXRF, calculated for Sally's values of $K = 0.345$ and $A = 0.27$. The coefficient decreases as pXRF force increases, up until the lines cut off at the point where the pXRF force would cause the robot's rear wheel to slip or lose contact.

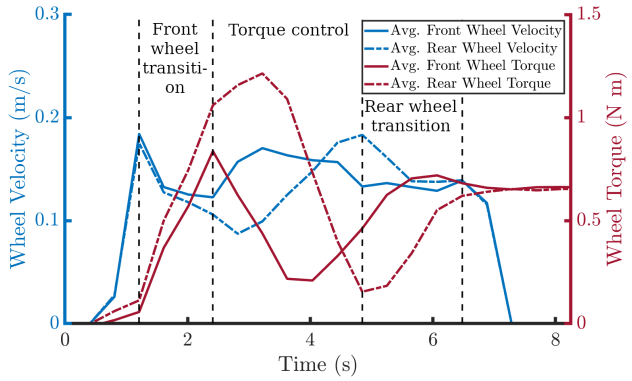

Fig. 6. Average front and rear wheel motor torques and velocities during a floor-to-wall transition. The robot's wheels are normally in velocity mode, but switch to torque for the duration between the front and rear wheel transitions.

previous surface near the end of the transition but before the rear wheels reach the corner. For floor-to-wall and wall-to-floor transitions the robot will naturally pivot around the front wheels until the rear wheels regain contact, but for wall-to-wall, wall-to-ceiling, and ceiling-to-wall transitions this can result in the robot pivoting away from the wall and falling.

With accurate state estimation it would be possible to vary the wheel speeds over the course of the transition and avoid this problem. However, a more robust solution is to use torque control on the wheels between the front wheels breaking contact and the rear wheels making contact, with a relatively low torque setpoint for the front wheels. This ensures that the force exerted by the front wheels will never be sufficient to prematurely pull the robot free of the previous surface. Notably, this solution only requires knowledge of the robot's contact state, rather than the exact angle of progress through the transition (as encoder-based measurements may become inaccurate due to wheel slip). Fig. 6 demonstrates the velocity and torque seen by the front and back motors during a floor-to-wall transition.

IV. Mobility Experiments

A. Interior Corner and Obstacle Traversal

We attempted all 7 interior corner transition types with fresh grip tape on the wheels, finding that Sally is capable of completing all but the wall-to-non-ferrous-floor transition without assistance from the steering motors or pXRF elevator. However, with the transition strategies described above, Sally was able to complete this transition as well. Key frames from each transition are shown in Fig. 7a-c. After repeated trials, the floor-to-wall transition began to require the use of wheel twisting as the grip tape lost traction due to wear.

We also evaluated obstacle traversal while driving on a vertical wall. Two types of obstacle were examined for each test: a segment of 3.8 cm square steel channel and a 5 cm diameter steel pipe. In the first test, each obstacle was placed to obstruct only one side of the drivetrain as a test of the rocker suspension. Sally successfully traversed both obstacles unaided, although the pXRF had to be raised to clear the obstacle. In the second test, each obstacle was placed to obstruct both wheels. Transitioning the back wheels over the obstacle proved challenging, because unlike in a wall-to-ceiling transition the moment due to gravity opposes the wheel breaking free from the wall. Sally was ultimately able to traverse these obstacles as well by applying the pXRF pushing and wheel twisting strategies (Fig. 7d-e).

B. Field Deployment

Sally was also tested at an industrial site which possessed several decommissioned structures available for robot testing, see Fig. 1 and the video attachment. In particular, the experiments included climbing: 1) the exterior of a large water storage tank, where Sally was able to drive along the curved surface in any direction, over small bumps and welds, and take point and line scans using the pXRF (Figs. 1a and 10c); 2) a steel I-beam, on which Sally demonstrated a non-ferrous-floor-to-wall transition, point measurement, and wall-to-non-ferrous-floor transition (Fig. 1b); 3) a steel truckbed, on which Sally demonstrated a ferrous-floor-to-wall and wall-to-ferrous-floor transition (Fig. 1c); 4) a 1.8 m diameter steel pipe, on which Sally demonstrated the ability to drive on the interior and exterior of curved surfaces (Fig. 1d and e); and 5) the exterior of a shipping container, on which Sally demonstrated the ability to drive on non-flat surfaces (Fig. 1f).

Overall, Sally was able to successfully navigate all of these obstacles. Despite these successful demonstrations, several challenges became evident when Sally was taken to a field deployment environment. The most significant is the build up of loose magnetized dirt and rust on the outside of the wheels. This causes a reduction in adhesion, and large enough chunks of material can prevent the wheels from spinning entirely. Another challenge comes from surface patches that have rusted through to the point that they become brittle and the wheel loses adhesion. Finally, Sally struggles to traverse closely spaced rivets because a wheel can pass between two neighboring rivets while the attached

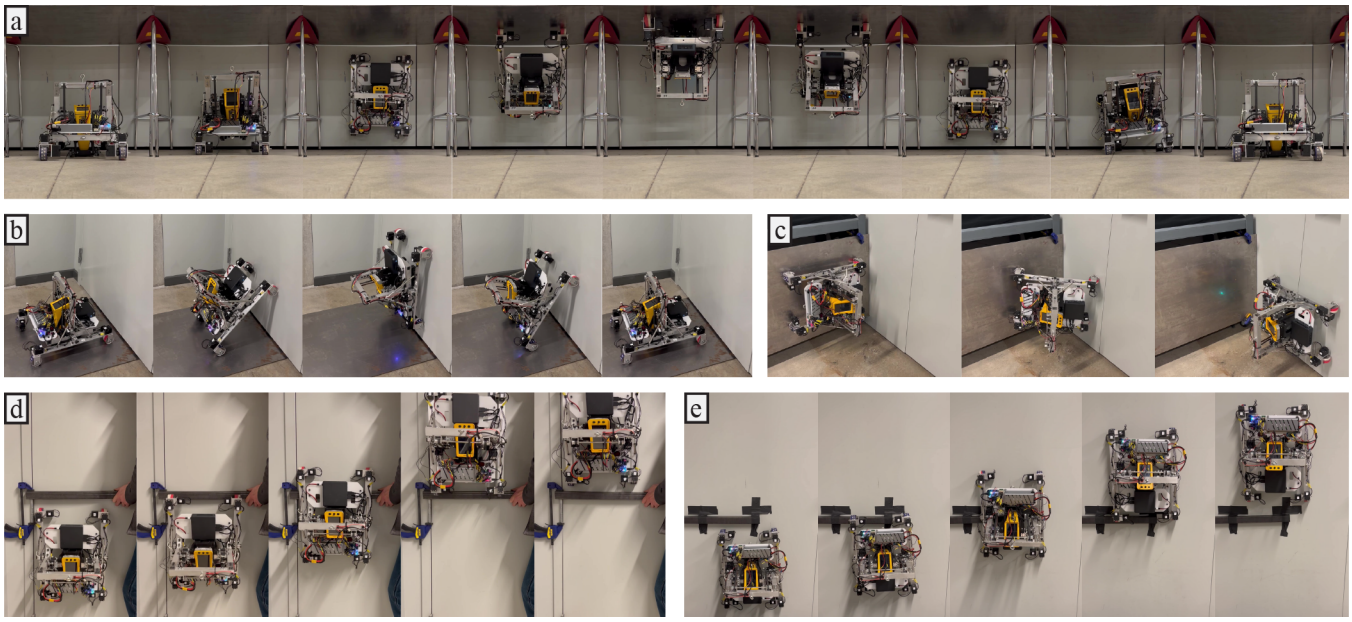

Fig. 7. Key frames taken during a) non-ferrous-floor-to-wall-to-ceiling-to-wall-to-non-ferrous-floor, b) wall-to-floor-to-wall, c) wall-to-wall, d) two-wheel obstacle (3.8 cm square steel channel) and e) one-wheel obstacle transitions.

drive motor collides with one of them. This issue likely extends to any set of obstacles with spacing wider than the wheel itself but narrower than the full wheel assembly.

V. Line Scanning Experiments

The pXRF surface sampling can be operated in two different ways: grid point measurement or line scanning. In traditional grid point measurement, the robot lowers the sensor to the ground and holds its position for the duration of the scan, resulting in a high-precision measurement of the elemental composition of the surface at a single location, which is similar to the way humans would in these tasks. In contrast, during line scanning, the robot drives at a constant velocity throughout the sensing, resulting in an average measurement of the surface composition along the line it travels with the same amount of time as point measurement does. For the surface inspection task, the goal is to find any remaining hot spots of target elements remaining after cleaning the surfaces. Thus, by taking line scans, the robot can relatively quickly cover large areas of the surface and only revisit locations to perform more precise point measurements when non-negligible concentrations of target elements (e.g. heavy metals) are detected. Line scanning is also effective if the study objective is to get an overall average concentration level for target elements, as it will give a more accurate average for the length of the line than a single scan.

A. Limit of Detection and Maximum Speed

To achieve an acceptable signal-to-noise ratio, it is important to determine the limit of detection (LOD) for the sensor. The pXRF sensor works by collecting the signal detected over time, so the LOD depends on the total scan time t. The LOD was estimated as 3.3 times the blank (i.e. clean sample) standard deviation over the pXRF calibration slope. The LOD is element-specific, but for 5, 20, and 80 second scans, the LOD for surface mercury are 0.4, 0.2 and 0.1 µg/cm^2, respectively. The LOD increases with $t^{-1/2}$. Since line scanning averages the signal it collects throughout the path, the maximum speed v_{max} depends on spot size ℓ_s, scan time t, LOD λ_t under this scan time, and the user-defined analysis threshold concentration C_{th}. Equation (17) describes this on-off constraint, assuming $C_{th} \geq \lambda$.

$$v_{max} = \frac{C_{th}}{\lambda_t} \cdot \frac{\ell_s}{t} \tag{17}$$

B. Comparison in Simulation

To better understand the performance of point measurement and line scanning, we performed simulations in randomly generated surface concentration maps using Python. The map generation method is discussed in [26] and the Monte Carlo method is applied here. Different numbers of point measurement and line scanning were tested in two different types of generated maps: one map with low heterogeneity, which means that the concentration distribution is more clustered, and one map with high heterogeneity, where the distribution is more scattered. Examples of each map type are shown in Fig. 8.

Each map type was generated a thousand times for Monte Carlo simulation and the average Error Rate for each sensing type was recorded for each type of map. The point measurement was simulated by using the value of the pixel in the generated map, and the line scanning was simulated by averaging all pixels on the line it travels through. Illustrations of each sensing type (point vs. line) are shown in Fig. 8. The true value is the average value of the entire map.

The results of simulations on randomly generated maps are shown in Fig. 9. The number of samples was varied from

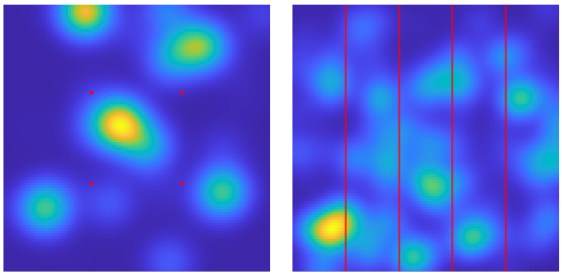

Fig. 8. Simulation maps with point measurement in low heterogeneity (left) and line scanning in high heterogeneity (right).

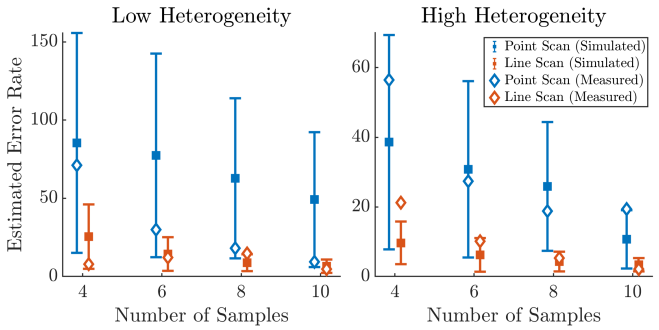

Fig. 9. Comparison of measurement error between point and line scanning methods. The solid markers and error bars show the mean and 90% confidence interval of measurements from simulation, while the hollow markers record the actual measurements collected by Sally.

4 to 10, and the line scan performed better on average in estimating the mean concentration in all cases. Each line scan takes the same sampling duration as a point measurement, so line scanning provides a better estimate of the area mean concentration in surface sensing for the same amount of time.

C. Lab Experiments

To validate the simulation results, real surfaces with known surface Hg concentrations and distributions were created by painting the surface with latex paint containing a known amount of HgS(s) particles on two 127 cm x 127 cm sheets of paper. One of them was painted with a lower heterogeneity and one with a higher heterogeneity.

The true mean of the maps was determined using a 5x5 grid of 30 second point measurements. Then, different numbers of samples (4, 6, 8, 10) for both line scanning and point measurements were taken by the Sally robot (Fig. 10a).

The results of the two maps were compared with the

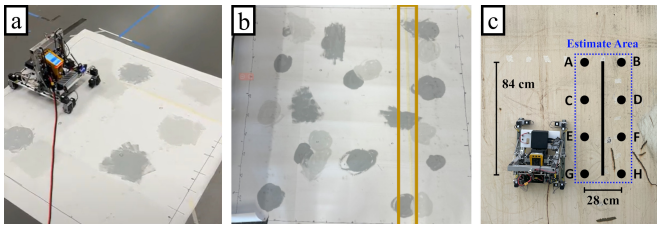

Fig. 10. Experimental sampling method comparisons. a) The robot shown on a low heterogeneity painted map. b) The high heterogeneity map with the region sampled for the line scan duration experiments marked. c) The robot at the field site with the sample locations marked.

Sampling Method	Duration (s)	Hg ($\mu g/cm^2$)	SD ($\mu g/cm^2$)
Point measurement	30	0.45	0.41
Line scanning at 2.1 cm/s	60	0.43	0.07
Line scanning at 4.2 cm/s	30	0.41	0.10
Line scanning at 8.5 cm/s	15	0.33	0.15

TABLE I

THE INFLUENCE OF THE SPEED ON LINE SCANNING

simulation results in Fig. 9. The real-world experimental results align with the simulations: most of the data points fall within the 90% confidence intervals shown on the figure, and we again see the improved performance of line scanning for determining the area mean estimate compared to the same number of point measurements.

D. Scan Speed Experiments

Line scanning can be seen as the average of all point measurements across a line, where the speed of the line scan influences the precision of the results. To demonstrate this, we used Sally to make 45 point measurements in a line on the high heterogeneity map (Fig. 10b). We then attempted line scanning at three different speeds: high: 8.5 cm/s, medium: 4.2 cm/s, and low: 2.1 cm/s, along the same line, repeating each speed three times. The results are shown in Table I. As the speed decreases, the standard deviation decreases and the mean concentration converges toward the ground truth value obtained via point sampling.

E. Field Environments

Sally performed a sensing comparison test on the exterior of a water storage tank at an industrial site, where eight grid point measurements and one line scan were recorded for the concentration of Zn (Fig. 10c). We use the average value of all eight point measurements, 0.58 $\mu g/cm^2$, as the true area mean we want to measure. Compared to each individual point measurement of the same time duration, the line scan method reduced the average measurement error from 58.50% to 36.48%, a 37.60% reduction. While the accuracy can be further improved in either case to meet application requirements by increasing the scan duration or number of samples, these results support the conclusion from simulation and lab experiments that line scanning gives a better estimate of the area mean than point sampling for the same amount of sampling time.

VI. Discussion and Conclusion

In this work, we introduce the first magnetic-wheeled wall climbing robot that is capable of executing all possible interior corner transitions. As predicted by the model, with only the drive actuators Sally is able to complete all transition types except for the wall-to-non-ferrous-floor transition without pXRF pushing and wheel twisting. However, one of the keys to Sally's effectiveness lies in the dual-use of the robot's mechanisms, such as the pXRF elevator and steering actuators, in order to complete all interior corner transition types successfully. In actual deployment, a lower friction coefficient is a safer and more realistic assumption, and thus

the two supplemental techniques are critical for ensuring reliable mobility even when performance is degraded. Additionally, the independent steering mechanism grants high maneuverability that is ideal for operating in tight spaces.

Sally was successfully deployed at a field site where we were able to demonstrate many of the key features of the design. These tests also helped to identify areas for further research and development. The accumulation of magnetized dirt on the wheels, although of less concern in a relatively clean oil tanker setting, is a critical issue in dirty or corroded environments and a self-cleaning solution that scrapes off excess material would be extremely valuable. An active suspension would improve Sally's ability to regain contact in the event that a wheel loses adhesion. Using larger wheels or offsetting the drive motors upwards would improve performance when driving over closely spaced rivets.

The line scanning technique, enabled by Sally's wheeled design, offers a more efficient way to estimate distributions in industrial cleaning or inspection applications. We demonstrate that line scanning provides a more accurate estimate of the area mean than traditional point measurements over the same period of time, both in simulation and field deployment. However, scans occasionally fail because of unevenness on the surface, triggering a safety setting within the sensor. This failure mode may be partially addressed by carefully controlling the elevator, but ultimately limits the technique to fairly smooth surfaces (with the robot's obstacle and corner maneuverability valuable for transitioning between these surfaces). Despite this limitation, line scanning has the potential to provide significant time savings across a wide array of tasks as robotic solutions become more prevalent.

The current interior corner transition model assumes quasi-static motion and a straight-on approach, but by using the robot's momentum or approaching at an angle, one wheel at a time, it may be possible to achieve transitions even with a much lower tire friction coefficient. Generalizing the transition model to a 6-wheeled robot could similarly enable greater reliability. Finally, traversing interior corners and obstacles with Sally requires a teleoperator to remember a sequence of operations (e.g. push with pXRF, switch to torque mode, switch back to velocity mode, twist rear wheels), where an incorrect command can cause the robot to lose adhesion and fall. It would be valuable to develop driver-assist features that automate this logic, reducing the burden on the teleoperator and paving the way for a fully autonomous solution that uses an onboard camera or lidar to build up a 3D map of component concentrations.

REFERENCES

[1] A. Sirken, G. Knizhnik, J. McWilliams, and S. Bergbreiter, "Bridge risk investigation diagnostic grouped exploratory (BRIDGE) bot," in *IEEE/RSJ International Conference on Intelligent Robots and Systems*, 2017, pp. 6526–6532.

[2] P. A. Bogdan, J. Wheadon, F. B. Klein, and M. Gianni, "Magnetic tracked robot for internal pipe inspection," in *European Conference on Mobile Robots*, 2021, pp. 1–6.

[3] A. Shukla and H. Karki, "Application of robotics in onshore oil and gas industry-a review part I," *Robotics and Autonomous Systems*, vol. 75, pp. 490–507, 2016.

[4] F. Bonnin-Pascual and A. Ortiz, "On the use of robots and vision technologies for the inspection of vessels: A survey on recent advances," *Ocean Engineering*, vol. 190, p. 106420, 2019.

[5] V. Nava, N. Sihota, T. Hoelen *et al.*, "Portable X-ray fluorescence for autonomous in-situ characterization of chloride in oil and gas waste," *Environmental Pollution*, vol. 316, p. 120558, 2023.

[6] J. Norby, S. Wang, H. Wang *et al.*, "Path to autonomous soil sampling and analysis by ground-based robots," *Journal of Environmental Management*, vol. 360, p. 121130, 2024.

[7] W. Myeong, S. Song, and H. Myung, "Development of a wall-climbing drone with a rotary arm for climbing various-shaped surfaces," in *International Conference on Ubiquitous Robots*, 2018, pp. 687–692.

[8] J. Hu, X. Han, Y. Tao, and S. Feng, "A magnetic crawler wall-climbing robot with capacity of high payload on the convex surface," *Robotics and Autonomous Systems*, vol. 148, p. 103907, 2022.

[9] S. Hong, Y. Um, J. Park, and H.-W. Park, "Agile and versatile climbing on ferromagnetic surfaces with a quadrupedal robot," *Science Robotics*, vol. 7, no. 73, p. eadd1017, 2022.

[10] T. Bandyopadhyay, R. Steindl, F. Talbot *et al.*, "Magneto: A versatile multi-limbed inspection robot," in *IEEE/RSJ International Conference on Intelligent Robots and Systems*, 2018, pp. 2253–2260.

[11] S. T. Nguyen, A. Q. Pham, C. Motley, and H. M. La, "A practical climbing robot for steel bridge inspection," in *IEEE International Conference on Robotics and Automation*, 2020, pp. 9322–9328.

[12] Y. Bu, Y. Bu, H. Li *et al.*, "Development of wheel-leg hybrid climbing robot with switchable permanent magnetic omni-wheels as feet," in *IEEE International Conference on Robotics and Biomimetics*, 2022, pp. 1–6.

[13] J. Quan, M. Zhu, and D. Hong, "A lightweight mobile robot for climbing steel structures with an extending and bending tape spring limb," in *ASME International Design Engineering Technical Conferences and Computers and Information in Engineering Conference*, vol. 8: 47th Mechanisms and Robotics Conference, 2023, p. V008T08A084.

[14] R. Wang and Y. Kawamura, "Development of climbing robot for steel bridge inspection," *Industrial Robot: The International Journal of Robotics Research and Application*, vol. 43, no. 4, p. 429–447, 2016.

[15] H. Eto and H. H. Asada, "Development of a wheeled wall-climbing robot with a shape-adaptive magnetic adhesion mechanism," in *IEEE International Conference on Robotics and Automation*, 2020, pp. 9329–9335.

[16] B. Wang, P. Li, P. Li *et al.*, "Development of a wheeled wall-climbing robot with an internal corner wall adaptive magnetic adhesion mechanism," *Journal of Field Robotics*, pp. 1–18, 2024.

[17] US EPA, OLEM. Tank inspections. [Online]. Available: https://www.epa.gov/oil-spills-prevention-and-preparedness-regulations/tank-inspections

[18] Z. Y. Soon, J.-H. Jung, C. Yoon *et al.*, "Characterization of hazards and environmental risks of wastewater effluents from ship hull cleaning by hydroblasting," *Journal of Hazardous Materials*, vol. 403, 2021.

[19] E. Akyuz and M. Celik, "A methodological extension to human reliability analysis for cargo tank cleaning operation on board chemical tanker ships," *Safety Science*, vol. 75, pp. 146–155, 2015.

[20] S. Wickramanayake, K. Thiyagarajan, S. Kodagoda, and L. Piyathilaka, "Ultrasonic thickness measuring in-pipe robot for real-time non-destructive evaluation of polymeric spray linings in drinking water pipe infrastructure," *Mechatronics*, vol. 88, p. 102913, 2022.

[21] A. Gunatilake, L. Piyathilaka, A. Tran *et al.*, "Stereo vision combined with laser profiling for mapping of pipeline internal defects," *IEEE Sensors Journal*, vol. 21, no. 10, pp. 11 926–11 934, 2021.

[22] J. Valls Miro, N. Ulapane, L. Shi *et al.*, "Robotic pipeline wall thickness evaluation for dense nondestructive testing inspection," *Journal of Field Robotics*, vol. 35, no. 8, pp. 1293–1310, 2018.

[23] M. Tavakoli, C. Viegas, L. Marques *et al.*, "OmniClimbers: Omni-directional magnetic wheeled climbing robots for inspection of ferromagnetic structures," *Robotics and Autonomous Systems*, vol. 61, no. 9, pp. 997 – 1007, 2013.

[24] W. Fischer, F. Tâche, G. Caprari, and R. Siegwart, "Magnetic wheeled robot with high mobility but only 2 DOF to control," in *Advances In Mobile Robotics*. World Scientific, 2008, pp. 319–328.

[25] C. Park, J. Bae, S. Ryu *et al.*, "R-Track: Separable modular climbing robot design for wall-to-wall transition," *IEEE Robotics and Automation Letters*, vol. 6, no. 2, pp. 1036–1042, 2021.

[26] H. He, J. Norby, S. Wang *et al.*, "Environmental sampling with the boustrophedon decomposition algorithm," arXiv, Tech. Rep. arXiv:2207.06209 [cs.RO], 2022.